Modelling mixed columnar-equiaxed solidification with melt convection and grain sedimentation – Part II: Illustrative modelling results and parameter studies

M. Wu *, A. Ludwig, A. Fjeld

Simulation and Modelling of Metallurgical Processes, Department of Metallurgy, University of Leoben, A-8700 Leoben, Austria

ARTICLE INFO

ABSTRACT

A volume-averaging multiphase solidification model was introduced in Part I. In Part II, illustrative simulations are made for two benchmarks, a unidirectional solidification benchmark and a cylindrical ingot casting, using a binary Al–Cu alloy. For the case of unidirectional solidification the competing growth of columnar and equiaxed structures, evolution of different phase regions, solute redistribution, and the influence of grain sedimentation and melt convection are analyzed in detail. The columnar-to-equiaxed transition (CET) is investigated, with important insights derived from the CET prediction. The new features of the model and its applicability to industrial-type castings are demonstrated with simulations of a cylindrical ingot casting. This is done in both a 2D axisymmetric and a full 3D geometric domain to demonstrate the ability of the model to produce consistent results. The main features of the model that are verified include tracking of the columnar primary dendrite tip, nucleation of equiaxed grains ahead of the columnar tip front, hydrodynamic and solutal interactions between the equiaxed and columnar structures, the columnar-to-equiaxed transition (CET), melt convection and grain sedimentation, and macrosegregation and the final macrostructure. With appropriate modelling parameters the typical columnar-equiaxed macrostructure observed in experiments can be reproduced. Uncertainties due to model parameters and assumptions are addressed and discussed.

1. Introduction

In the last century significant progress has been made in describing the formation of the mixed columnar-equiaxed macrostructure, however the ability to control and dictate the as-cast macrostructure in a casting or ingot remains a challenge for metallurgists and foundrymen. Modelling efforts of the previous decades [1–4] have elucidated many aspects of the interdependent phenomena in columnar-equiaxed solidification, but due to the complex interaction of the multiphase flow and grain sedimentation during solidification and constraint of computing resources, modelling mixed columnar-equiaxed solidification at the process scale has not been fully realized and remains a problem under much current investigation.

Significant advances in modelling of dendritic alloys were made with the contributions of Rappaz and Thevoz [5,6] who proposed a micro–macro solute diffusion model for equiaxed dendritic solidification. Following this work Wang and Beckermann [7,8] suggested a multiphase approach encompassing either equiaxed or columnar solidification, in which a volume averaging method is used to model global multiphase transport phenomena including

flow and grain sedimentation. Recently, Ciobanas and Fautrelle [9,10] proposed an ensemble-averaged multiphase Eulerian model for mixed columnar-equiaxed solidification, although convection and grain sedimentation were not taken into account. Building upon the major features of these works, an expanded model, which encompasses mixed equiaxed-columnar solidification, convection and grain sedimentation, and tracks the evolution of dendritic morphologies has been presented by the current authors and is demonstrated here.

As stated in Part I, a model for mixed columnar-equiaxed solidification should bridge the macro and micro length scales, encompass both dendritic and non-dendritic morphologies, track the columnar primary dendrite tip front (which separates the pure equiaxed solidification zone from the mixed columnar-equiaxed solidification zone), and simulate multiphase flow and grain sedimentation. To incorporate these phenomena into a single model a volume-averaging multiphase solidification model with five thermodynamic phase regions is proposed. These five phase regions include the solid dendrites and the interdendritic melt in equiaxed grains, the solid dendrites and the interdendritic melt in columnar trunks, and the extradendritic melt. For melt flow and grain sedimentation, three hydrodynamic phases are defined: equiaxed grains, composed of solid dendrites and interdendritic melt; columnar dendrite trunks, composed of solid dendrites and

---

* Corresponding author.
  E-mail address: menghuai.wu@mu-leoben.at (M. Wu).

Nomenclature

c_0	initial (nominal) concentrations of alloy (wt.%)
c_E	eutectic concentration (wt.%)
c_ℓ, c_e, c_c	concentrations of hydrodynamic ℓ-, e-, or c-phases (wt.%)
$\bar{c}_{env}^c$	average concentration at columnar tree trunk envelope (wt.%)
$\bar{c}_{env}^e$	average concentration at equiaxed grain envelope (wt.%)
c_d^c, c_s^c	concentrations of interdendritic melt and solid dendrites in columnar tree trunk (wt.%)
c_d^e, c_s^e	concentrations of interdendritic melt and solid dendrites in equiaxed dendritic grain (wt.%)
c_{mix}	mix concentration (wt.%)
c_ℓ^*, c_s^*	equilibrium concentration at liquid–solid interface (wt.%)
$c_{p,\ell}, c_{p,s}$	specific heat of liquid and solid (J kg^{-1} K^{-1})
D_ℓ, D_s	diffusion coefficient in liquid or solid phase (m^2 s^{-1})
d^c	average diameter of columnar tree trunk (m)
d^e	average diameter of equiaxed grain diameter (m)
f_ℓ, f_e, f_c	volume fraction of hydrodynamic ℓ-, e-, or c-phases (1)
f_s^c, f_d^c	volume fraction of solid dendrites or interdendritic melt in columnar tree trunk referring to total volume (1)
f_s^e, f_d^e	volume fraction of solid dendrites or interdendritic melt in equiaxed grain referring to total volume (1)
f_c^{free}	critical volume fraction of columnar phase for entrapment of equiaxed grains (1)
$f_{e,CET}$	hard blocking criterion (Hunt model) (1)
f_{Eu}^{extra}	extradendritic eutectic phase (1)
$f_{Eu,e}^{intern}, f_{Eu,c}^{intern}$	interdendritic eutectic phases in equiaxed or columnar phase (1)
f_{Eu}^{total}	total eutectic phase (1)
g	gravity (m s^{-2})
G	temperature gradient at the columnar primary dendrite tip (K cm^{-1})
H_w	heat transfer coefficient at casting-chill interface (W m^{-2} K^{-1})
k	solute partitioning coefficient at the liquid–solid interface (1)
k_1	growth parameter in KGT model (m s^{-1} K^{-2})
k_2	growth parameter in KGT model (m s^{-1} K^{-3})
k_ℓ, k_e, k_c	thermal conductivity (W m^{-1} K^{-1})
L	latent heat (J kg^{-1})
l_ℓ	diffusion length around grain/trunk envelope (m)
m_ℓ	liquidus slope of binary phase diagram (K)
$M_{\ell e}(=-M_{e\ell})$	liquid-equiaxed net mass transfer rate (kg m^{-3} s^{-1})
$M_{\ell c}(=-M_{c\ell})$	liquid-columnar net mass transfer rate (kg m^{-3} s^{-1})
M_{ds}^c	interdendritic solidification rate in columnar trunk (kg m^{-3} s^{-1})
M_{ds}^e	interdendritic solidification rate in equiaxed grain (kg m^{-3} s^{-1})
n_{max}	maximum equiaxed grain density, or maximum available nucleation sites in heterogeneous nucleation law (m^{-3})
T_0	initial temperature (K)
T_f	melting point of pure metal (Al) (K)
T_L	liquidus temperature (K)
T_ℓ, T_e, T_c	temperatures of hydrodynamic ℓ-, e-, or c-phases (K)
T_E	temperature of eutectic reaction (K)
T_w	mould temperature (K)
ΔT	undercooling (K)
ΔT_c	undercooling at the columnar primary dendrite tip (K)
ΔT_N	undercooling for maximum grain production rate (K)
ΔT_σ	Gaussian distribution width of nucleation law (K)
$\vec{u}_\ell, \vec{u}_e, \vec{u}_c$	velocity vector of hydrodynamic ℓ-, e- or c-phase (m s^{-1})
v_{env}	growth velocity of the volume-equivalent envelope (m s^{-1})
$v_{tip'}^c$	growth velocity of columnar primary dendrite tip (m s^{-1})
α_d^c, α_s^c	volume fraction of interdendritic melt, solid dendrites inside the columnar tree trunks ($\alpha_d^c + \alpha_s^c = 1$) (1)
α_d^e	volume fraction of interdendritic melt inside equiaxed grains (1)
α_s^e	volume fraction of solid inside equiaxed grains ($\alpha_d^e + \alpha_s^e = 1$)
β_T	thermal expansion coefficient (K^{-1})
β_c	solutal expansion coefficient (1)
β_s	solidification volume shrinkage (1)
Φ_{circ}^c	circularity of the envelope of the columnar dendrite trunk (1)
Φ_{env}^c	shape factor of columnar dendrite trunk (1)
Φ_{env}^e	shape factor of equiaxed dendritic grain (1)
Φ_{sph}^e	sphericity of equiaxed grain envelope (1)
Γ	Gibbs–Thomson coefficient (m K)
λ_1	primary dendrite arm space of columnar tree trunk (m)
λ_2	secondary dendrite arm space (m)
μ_ℓ	viscosity (kg m^{-1} s^{-1})
$\rho_\ell, \rho_e, \rho_c$	average densities of hydrodynamic ℓ-, e-, or c-phases (kg m^{-3})
$\rho_\ell^{ref}, \rho_e^{ref}$	reference densities of extradendritic melt and equiaxed phase (kg m^{-3})
ρ_s	density of pure solid dendrite (kg m^{-3})

interdendritic melt; and the extradendritic melt. As the columnar dendrite trunks generally move with a predefined velocity, only two set of momentum conservation equations are solved for the flow of the extradendritic melt and the movement of the equiaxed grains. The interdendritic melt inside the equiaxed grains is assumed to move with the equiaxed grains, and the interdendritic melt inside the columnar trunks moves with the columnar dendrite trunks.

A major focus area of research in mixed columnar-equiaxed solidification is the columnar-to-equiaxed transition (CET). Numerous previous investigations of the CET were carried out under a relatively simple condition/assumption, i.e. the unidirectional solidification. Hunt [11] based on a 1D analytical model has suggested that CET might occur when the volume fraction of equiaxed grains ahead of the columnar primary dendrite tip front exceeds a critical value of $f_{e,CET} = 0.49$, known as hard blocking mechanism. Based on this assumption he successfully established a CET map: a correlation of the columnar primary dendrite tip growth velocity $v_{tip'}^c$ with the local temperature gradient G at the moment when CET occurs. This CET map was later confirmed and further improved by including nucleation effects [12] and more precise growth kinetics and by incorporation of a multi-field system taking into account hard- and soft-blocking mechanisms [9,10,13–17]. Subsequent phase field and stochastic models have also confirmed the CET phenomenon in a unidirectional solidification configuration [18–20]. Indeed, phase field methods can provide almost all the necessary physical details of CET, though they are limited to domain scales at the microscopic level. In the mean time unidirectional solidification experiments were often accompanied to verify the above models or to help exploring new models. From the

experimental results people tried to abstract some more practical/empirical correlations, which can be used as indirect criteria to predict the CET in engineering castings [21–25]. Some successes were made, although most of them are limited to selected alloy system or special process conditions. As part of the verification of the current model, the classic unidirectional solidification is here simulated. The newly proposed 5-phase model would provide most of the necessary information for CET at the process scale.

Finally, a full 3D simulation and a 2D axis symmetric simulation of a cylindrical casting are presented. Consistency of both simulations will be proven. The predicted macrostructure, i.e. the distinct equiaxed zone and columnar zone separated by CET, can be compared with the experimentally observed as-cast macrostructure [3,26]. The purpose of presenting this preliminary calculation is to demonstrate the features of the current model. Further verifications by comparison with the experiments will be made in future.

2. Unidirectional solidification

2.1. Benchmark description

The transient unidirectional solidification process under consideration is shown in Fig. 1. The geometry is 2D, however 1D heat transfer is enforced with a constant heat transfer coefficient (H_w) at the metal-chill interface (left wall) and adiabatic boundary conditions for the three remaining walls. Non-slip boundary condition for momentum equations and non-flux boundary condition for species transport equations are applied for all walls. This configuration allows for effective analysis of model results and model assumptions as well as verification from the extensive previous experimental and theoretical research on unidirectional solidification. The casting is filled with liquid melt of initial temperature T_0 before solidification begins. Solidification of columnar dendrites grow from the chilled surface, against the direction of heat flow while nucleation of equiaxed grains occurs in front of the columnar primary dendrite tip front when the necessary undercooling is achieved. Simulations are carried out with and without melt convection and grain sedimentation to study the effects of these phenomena. As CET analysis is one of the main objectives of this investigation, Al–4.7 wt.% Cu is chosen as the model alloy, for
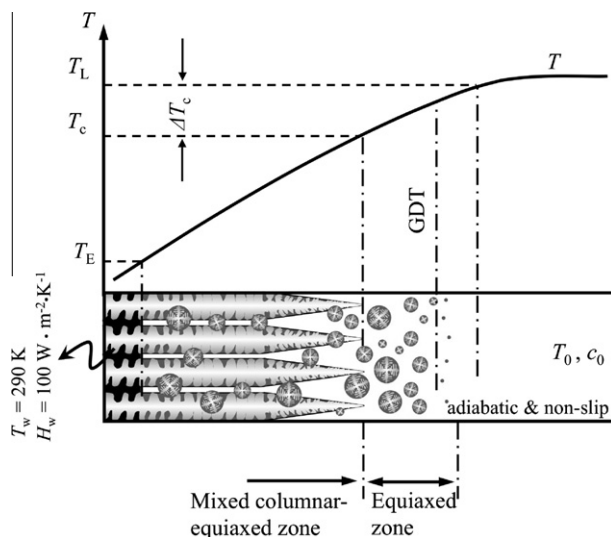
which substantial previous research on CET phenomenon in unidirectional solidification is available [16–19,25–27]. Well-defined thermo-physical and thermodynamic data are also widely available for this system.

Thermo-physical and thermodynamic properties, growth kinetics and dendritic morphological shape factors, together with the process conditions and nucleation parameters used for the current calculations are listed in Table 1. Sensitivity of the model to various process and model parameters is investigated by varying the heat transfer coefficient, nucleation parameters, and morphological shape factors. The influence of these parameters on solidification phenomena is discussed in detail in the following sections.

As a part of model verification, grid sensitivity studies are carried out under the casting conditions shown in Fig. 1 and Table 1 using a 1×1 mm^2 and a 0.5×0.5 mm^2 grid. In each case the time step is dynamically adapted to ensure that the convergent criteria mentioned in Part I are fulfilled at each time step. For the two mesh sizes all transport fields and solution variables are found to be in agreement and the predicted CET position is in very close agreement, with a CET at 44.5 mm from the chilled surface for the coarse grid and 43.25 mm for the fine grid. Thus, at these mesh sizes the results can be considered grid independent.

2.2. Evolution of phase regions

The distribution of columnar and equiaxed phases at t = 115 s is shown in Figs. 2 and 3, with the corresponding solute concentrations

Table 1
Parameters used for the process simulations.

Thermo-physical properties:
$\mu_\ell = 1.3 \times 10^{-2}$ kg m^{-1} s^{-1}
$c_{p,\ell}$ ($c_{p,s}$) = 1179 J kg^{-1} K^{-1}
$D_\ell = 3 \times 10^{-9}$ m^2 s^{-1}
$D_s = 8 \times 10^{-13}$ m^2 s^{-1}
$L = 3.97 \times 10^5$ J kg^{-1}
$k_\ell = 77$ W m^{-1} K^{-1}
$k_e(k_c) = 153$ W m^{-1} K^{-1}
$\rho_\ell(\rho_e, \rho_c) = 2606$ kg m^{-3}

Boussinesq parameters:
$\beta_T = 10^{-4}$ K^{-1}
$\beta_c = 9.2 \times 10^{-3}$ wt.%$^{-1}$
$\beta_s = (\rho_s - \rho_\ell)/\rho_e^{ref} = 0.0526$
$\rho_\ell^{ref}(\rho_e^{ref}) = 2606$ kg m^{-3}
$\rho_s = 2743$ kg m^{-3}

Growth kinetics parameters in KGT model [28,29]:
$k_1 = 1.16633 \times 10^{-4} \cdot (100 \cdot c_\ell)^{-1.24319}$
$k_2 = 5.39996 \times 10^{-4} \cdot (100 \cdot c_\ell)^{-2.13518}$

Thermodynamic parameters:
$k = 0.145$
$m_\ell = -344.0$ K
$T_f = 933.5$ K
$T_E = 821.4$ K
$c_E = 32.6$ wt.%
$\Gamma = 2.4 \times 10^{-7}$ m K

Nucleation parameters[a]:
$n_{max} = 1 \times 10^9$ m^{-3}
$\Delta T_N = 5$ K
$\Delta T_\sigma = 2$ K

Process conditions[a]:
$c_0 = 4.7$ wt.%
$T_0 = 932$ K
$H_w = 100$ W m^{-2} K^{-1}
$T_w = 290$ K

Morphological shape factors[a]:
$\Phi_{env}^e = 0.6827$ $\Phi_{sph}^e = 0.283$
$\Phi_{env}^c = 0.7979$ $\Phi_{circ}^c = 0.5$
$\lambda_1 = 500$ μm $\lambda_2 = 100$ μm

[a] Those parameters are varied for parameter study.

Fig. 1. Configuration of the unidirectional solidification benchmark. The calculation domain (100×10 mm^2) is meshed into 1000 rectangular volume elements of 1×1 mm^2. Calculation with a finer mesh (0.5×0.5 mm^2) has been repeated to verify the mesh independence of the numerical result.
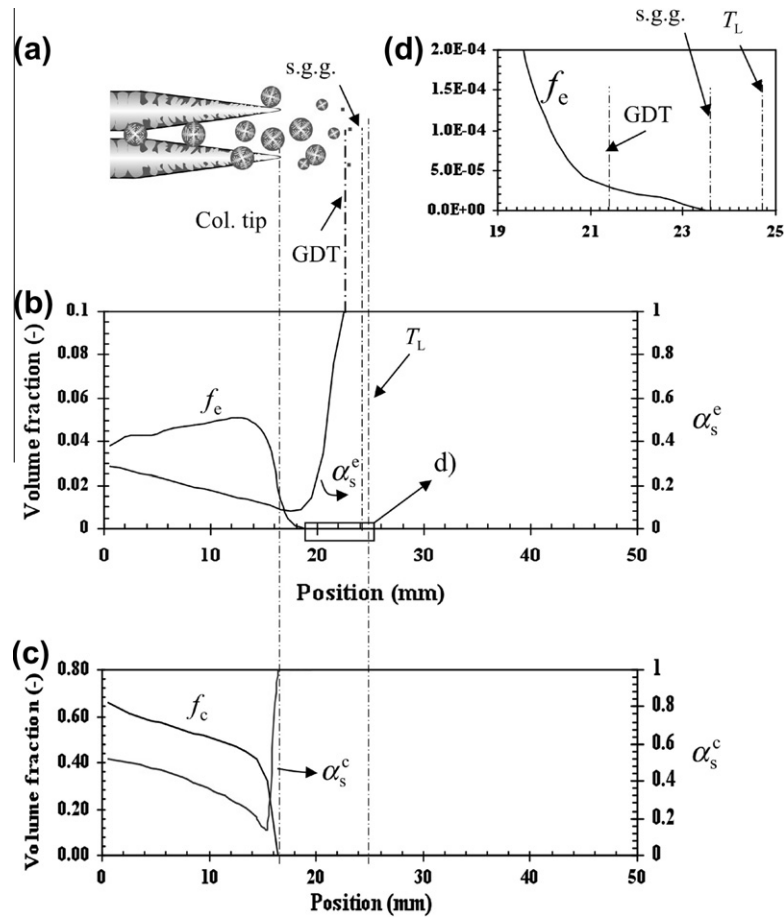
Fig. 2. Predicted distribution of columnar and equiaxed phases at 115 s (a) graphical depiction of the mixed columnar-equiaxed solidification, (b) volume fraction of hydrodynamic equiaxed phase, f_e, and the internal volume fraction of solid dendrites within the equiaxed phase α_s^e, (c) hydrodynamic columnar phase, f_c, and the internal volume fraction of solid dendrites within columnar phase, α_s^c, (d) close up view of GDT from b). The position of the liquidus isotherm, T_L, the start of globular grain growth (s.g.g.), the globular-to-dendritic transition (GDT), and the columnar primary dendrite tip position are indicated.

for each phase shown in Fig. 4. The phase and concentration distributions are taken along the middle line of the unidirectional solidification benchmark, which can represent distributions along any line parallel to the direction of heat transfer. Figs. 2 and 4 show the positions of the liquidus isotherm, the start of globular equiaxed grain growth (s.g.g.), the globular-to-dendritic transition (GDT), and the columnar primary dendrite tip front. Equiaxed nucleation is computed with a continuous 3-parameter nucleation law, in which nucleation can occur immediately below the liquidus temperature, but the nucleation rate is dependent on the local constitutional undercooling. For discussion purposes, however, the s.g.g. corresponds to a statistically significant number of grains which can be visually identified as $f_e > 0$ in Fig. 2d.

The columnar phase f_c begins to grow from the chilled surface with cellular morphology, i.e. solid fraction within the columnar phase, α_s^c, is 1, as soon as undercooling is achieved. In Fig. 2c α_s^c decreases sharply from 1 to 0.2 indicating an immediate transition from cellular to dendritic growth (CDT) at the columnar front. The position of the columnar primary dendrite tip front advances according to KGT growth kinetics (Part I) [28,29]. In the snapshot of Fig. 2 the columnar tip front is located 16.2 mm from the chilled surface, 8.5 mm behind the liquidus isotherm. Between the liquidus isotherm and the columnar tip front, equiaxed grains nucleate and grow as globular grains ($\alpha_s^e = 1$), 1.1 mm behind the liquidus isotherm. After a short interval of globular growth, GDT occurs at 21.4 mm from the chilled surface. Between the GDT position and the columnar dendrite tip front the volume fraction of the solid
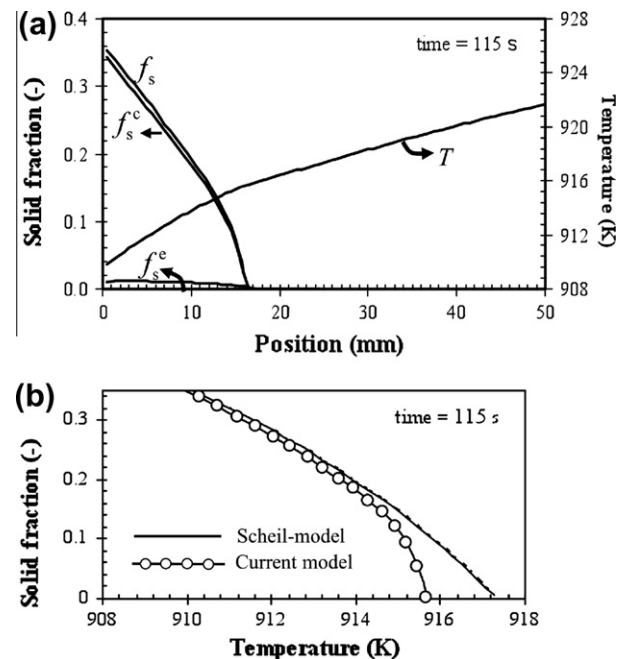

Fig. 3. Volume fraction distribution of solid phase and temperature field at 115 s showing (a) the total amount of solid f_s, equal to the sum of the solid dendrites within both the columnar trunks f_s^c and the equiaxed grains f_s^e and (b) the $f_s - T$ correlation obtained from the current model compared with the Scheil-model.
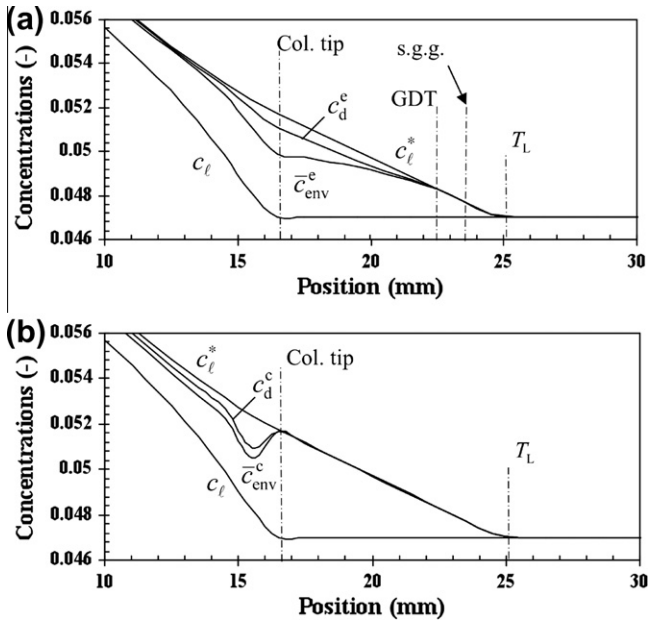
Fig. 4. Distribution of solute concentration in each liquid phase region near the primary dendrite tip at $t = 115$ s for (a) equiaxed phase and (b) columnar phase, where c_ℓ is the extradendritic melt concentration, c_d^c and c_d^e are solute concentrations of the interdendritic melts in the columnar trunks and equiaxed grains, $\bar{c}_{env}^c$ and $\bar{c}_{env}^e$ are average solute concentrations at the respective grain boundary envelopes, and c_ℓ^* is the liquid equilibrium concentration. The positions of T_L, s.g.g., GDT and columnar primary dendrite tip are indicated.

dendrites inside the grain envelope, α_s^e, drops rapidly from 1.0 to about 0.1, indicating that the equiaxed grains become highly dendritic. The volume fraction of equiaxed grains f_e at the columnar dendrite tip front, 0.025, is still quite low. In the inter-columnar space the equiaxed grains can continue to grow, although the growth velocity is very small. Accompanying above grain envelope growth processes, equiaxed interdendritic melt solidifies as well and the volume fraction of solid dendrites in the equiaxed grains α_s^e gradually increases.

At the mould wall the volume fractions of columnar and equiaxed phases are 0.64 and 0.04 respectively. Since the columnar primary dendrite tips grow from the mould wall, the small amount of equiaxed phase is assumed to form in the inter-columnar space. As shown in Fig. 3a, most of the solid formed near the mould wall consists of solid dendrites from the columnar trunks, while the equiaxed grains have only a small contribution to the total solid phase. Thus, the model is in agreement with the well-established pattern of dominant columnar dendritic growth near the casting surface. Further model validation is shown in the agreement of the predicted $f_s - T$ curve with the Scheil model in Fig. 3b. As is expected, the $f_s - T$ curve deviates from the Scheil model in the initial stage of solidification, where the Scheil model assumes complete mixing of the solute element in the liquid phase. This assumption has been shown to be a poor one in numerous previous investigations [5,6,27]; likewise the current model shows that the assumption of the complete solute mixing in the liquid phase is valid in general during solidification, but not in the initial stage.

Fig. 4 shows concentrations of the interdendritic and extradendritic melts at 115 s. The liquid equilibrium concentration, c_ℓ^*, which applies at the interface between the interdendritic melt and the solid dendrites, is determined by the local temperature according to the thermodynamic information of the phase diagram. The difference between c_ℓ^* and c_ℓ serves as the driving force (supersaturation) for nucleation and growth of equiaxed grains as well as the driving force for growth of the columnar primary den-

drite tips and for growth of columnar dendrite trunks in radial direction. The average concentration of the interdendritic melt is shown by c_d^e for equiaxed, and c_d^c for columnar. The difference between c_ℓ^* and c_d^e (or c_d^c) serves as the driving force for interdendritic melt solidification. $\bar{c}_{env}^e$ and $\bar{c}_{env}^c$ are average envelope concentrations, and they are important quantities for calculating the solute exchange between interdendritic melt and extradendritic melt. As the current model does not include melting and back diffusion, the solute concentration of solid dendrites is not discussed. Without resolving the microscopic details of each dendrite or dendritic grain, the above concentrations, together with quantities like average grain size d^e (or d^c), provide sufficient information to 'reconstruct' the characteristic solute distribution profile across the grain.

The modelling result (Fig. 4) shows that the supersaturation $(c_\ell^* - c_\ell)$ is established as soon as the local temperature drops below the liquidus temperature. c_ℓ^* increases with the decrease of temperature, while c_ℓ remains constant ($\sim c_0$) until the columnar primary dendrite tip front is reached. During globular equiaxed growth, there is no distinction among c_ℓ^*, c_d^e and $\bar{c}_{env}^e$, and enrichment of c_ℓ is minimal since the volume fraction of the globular grains is negligible. Following GDT the grain becomes dendritic, the growing envelope encloses extradendritic melt of average concentration of $\bar{c}_{env}^e$ into grain envelope, thus having an effect of decreasing the interdendritic solute concentration. In contrast, solute partitioning at the solid dendrite–interdendritic liquid interface during solidification increases the solute concentration of the interdendritic melt. The interdendritic melt concentration, c_d^e, is actually a result of these two competing phenomena. At the grain envelope two species exchange mechanisms exist in opposition, species diffusion from the interdendritic melt into the extradendritic melt and species transfer due to growth of the grain envelop, which encloses extradendritic melt with lower solute concentration into the interdendritic melt region. When the former one is dominant, the extradendritic melt becomes gradually enriched with solute element. When the later is dominant, the average concentration of the extradendritic melt may remain constant. The constant c_ℓ during pure equiaxed growth ahead of the columnar tip (Fig. 4) indicates that the later mechanism, i.e. species transfer due to growth of the grain envelop, dominates.

For the mixed columnar-equiaxed zone, the situation becomes more sophisticated. As mentioned previously (Fig. 2c), CDT occurs almost at the columnar tip front. Therefore, enclosure of the extradendritic melt of average concentration of $\bar{c}_{env}^c$ into the columnar trunk leads to immediate decrease of c_d^c from c_ℓ^*. In the deep mixed columnar-equiaxed zone, with the increasing distance from the columnar dendrite tip front the difference between $\bar{c}_{env}^c$, c_d^c and c_ℓ^* becomes smaller and smaller, because the growth of columnar trunk envelope is suppressed due to the impingement while the solidification of the interdendritic melt continues. The same situation happens to the equiaxed growth, where $\bar{c}_{env}^e$, c_d^e and c_ℓ^* get closer and closer. As the extradendritic melt is shared by the equiaxed and the columnar phases, the enrichment of the extradendritic melt is significant.

Martorano et al. [14] suggested that solute enrichment in the extradendritic melt due to growth of equiaxed grains ahead of the columnar tip front would exhaust the driving force (supersaturation) for columnar dendrite tip growth. The results in Fig. 4 show that this is not the case in the initial stages of solidification, because the small amount of equiaxed phase ahead of the columnar front is not sufficient to influence the extradendritic melt concentration. However, in the later stages of solidification, the effects of solutal impingement become more evident, as shown in Fig. 5 at $t = 275$ s. At the columnar tip front, $c_\ell^* = 0.0526$ and $c_\ell = 0.0486$, the extradendritic melt is significantly enriched in comparison with the initial concentration of 0.047. If the enrichment of c_ℓ is neglected, the driving force for the columnar primary dendrite tip
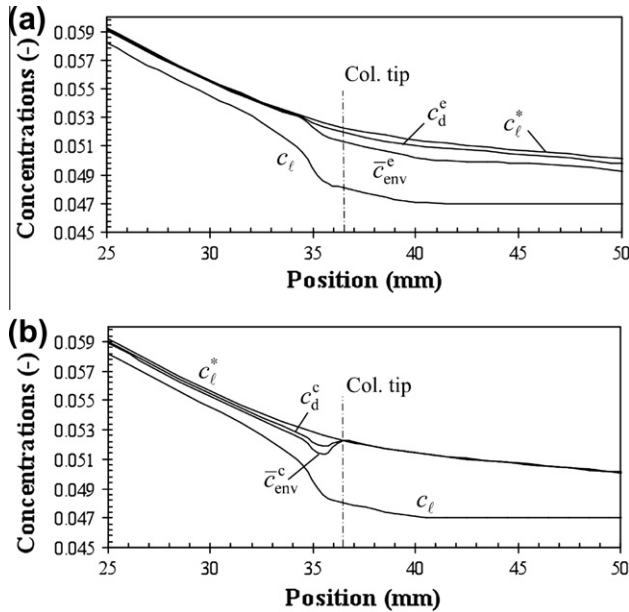
Fig. 5. Distribution of solute concentration in each liquid phase region near the columnar primary dendrite tip at $t = 275$ s. The columnar primary dendrite tip position is located at approx. 36.5 mm from the chilled surface.

growth $(c_\ell^* - c_\ell)$ would be overestimated by 28.6%. This solutal impingement effect on the columnar dendrite tip growth becomes even more important with the continuation of solidification.

The evolution of the interdendritic and extradendritic melt concentrations (Figs. 4 and 5) is the result of a series of coupled and competition phenomena which include solidification of the interdendritic melt and growth of the grain envelopes; solute partitioning at the solid–liquid interface and solute exchanges at the grain envelope; and competing growth between equiaxed grains and columnar trunks. These complex interactions are included in the current model, which is described in detail in Part I.

2.3. CET phenomenon

Fig. 6 shows the dynamic evolution of the hydrodynamic columnar phase, f_c, and equiaxed phase, f_e. As solidification proceeds, the volume fraction of equiaxed grains ahead of the columnar primary dendrite tip front continually increases. At $t = 428$ s, the equiaxed volume fraction at the columnar dendrite tip front reaches the critical value of $f_{e,CET} = 0.49$ and the columnar primary dendrite tips are blocked by the equiaxed grains, i.e. the hard blocking mechanism takes effect and the growth velocity of the columnar primary dendrite tips is forced to zero. For the process conditions of the current investigation, the CET position is predicted approximately 44.5 mm from the chilled surface. Although the growth of the columnar primary dendrite tips is ultimately inhibited by the equiaxed grains as $f_{e,CET}$ limit is exceeded, the CET is induced due to both hard and soft-blocking mechanisms. As discussed previously (Fig. 5), in the later stages of solidification columnar tip growth velocity is significantly reduced due to solute enrichment ahead of the columnar tip front, as the solidifying equiaxed dendrites reject solute directly into the interdendritic melt which is further transported to the extradendritic melt. Additional evidence of the influence of equiaxed grains on columnar tip growth is shown in Fig. 7. As the volume fraction of equiaxed grains ahead of the columnar tip increases, the influence of solutal impingement and thermal impingement (release of equiaxed latent heat) increases, and the columnar tip growth velocity, $v_{tip'}^c$, decreases. The thermal hindrance, or reduction of the cooling rate, at the columnar tip comes from the growing distance of the tip from the mould wall.
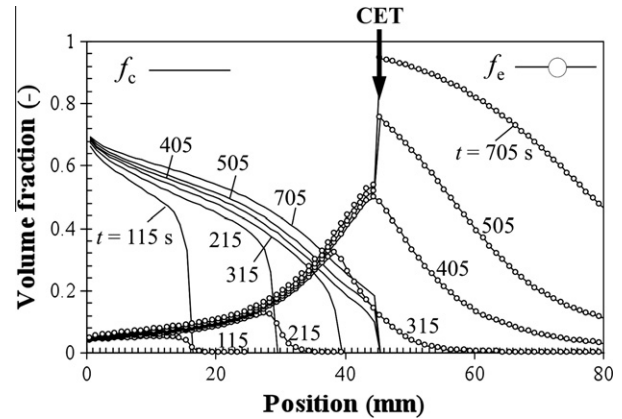
Fig. 6. Evolution of the columnar and equiaxed phases. The CET occurs at 428 s, approximately 44.5 mm from the mould wall.
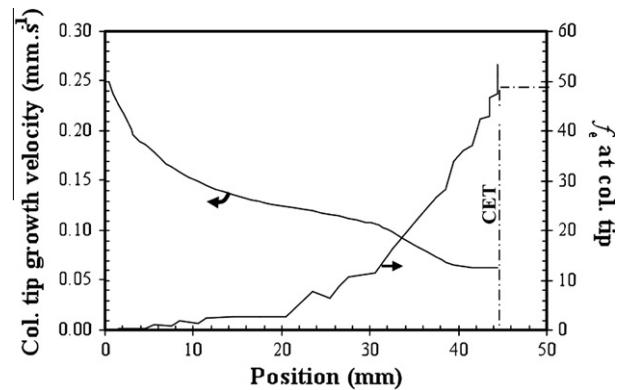

Fig. 7. Columnar primary dendrite tip growth velocity $v_{tip'}^c$ and the equiaxed volume fraction f_e at the columnar primary dendrite tip as function of columnar primary dendrite tip position.

To further explore the CET phenomenon, 30 simulations with varying process parameters are analyzed (superheat: 5, 15, 30, 50, 75, 100 K, and heat transfer coefficient: 50, 100, 200, 500, 1000, 2000, 4000 W m^{-2} K^{-1}). Each simulation is run until CET occurs. Fig. 8 charts the log of columnar tip growth velocity, $v_{tip'}^c$, and log of temperature gradient, G, for each of these simulations at the moment when CET occurs. Independent of the chosen process parameters, all the CET points fall within a narrow band in this log($v_{tip'}^c$)-log(G) plot. These gray bands divide the plot area into columnar-equiaxed growth in the lower-right and pure equiaxed growth in the upper-left. This result agrees well with previous studies [1,11,17]. With an increasing maximum number density of equiaxed nuclei, n_{max}, from 1×10^9 m^{-3} to 5×10^{10} m^{-3}, our model predicts a shift of the CET band towards the lower-right corner of the plot, again in agreement with the Hunt's model [11,17]. Note that many analytical studies on CET are based on a quasi-steady state condition with an imposed growth velocity, $v_{tip'}^c$, and an imposed temperature gradient, G. In the present model only the process parameters are imposed, whereas $v_{tip'}^c$ and G are obtained as modelling results of a transient simulation. In the current range of the process parameters, $v_{tip'}^c$ and G are found to fall into a relatively narrow range in comparison to previous analytical studies that specified $v_{tip'}^c$ and G [1,11,12].

2.4. Columnar growth vs. mixed columnar-equiaxed growth

As an alternative to specifying a blockage criterion for CET prediction, methods have been proposed which use indirect criteria based on a columnar-front-tracking model [21–24]. However,
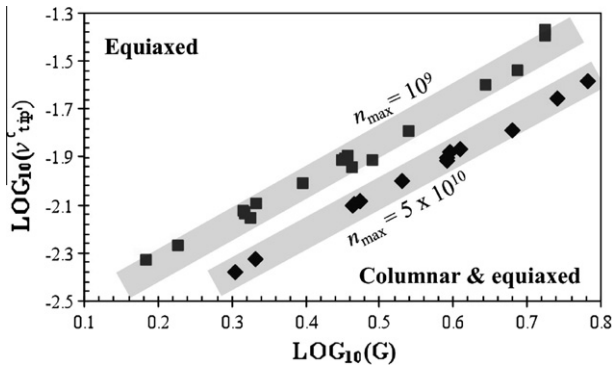
Fig. 8. Predicted CET map for an Al–4.7 wt.% Cu alloy. The columnar primary dendrite tip growth velocity, $v_{tip'}^c$ (cm s^{-1}), and the temperature gradient, G (K cm^{-1}), are taken at the columnar primary dendrite tip at the moment when CET occurs. A heterogeneous, 3-parameter Gaussian nucleation law is used with parameters, $\Delta T_N = 5$ K, $\Delta T_\sigma = 2$ K, and n_{max}, are shown in the diagram.

these models do not account for equiaxed growth. For instance, Gandin [21] found that the CET coincided with the point at which the local maximum dendrite growth velocity and the constrained-to-unconstrained (positive temperature gradient to negative temperature) transition occurred. Browne et al. [23] have combined the columnar-front-tracking model with a peak equiaxed index criterion with CET prediction results which show some agreement with experiments. Those studies, however, have also pointed out that neglect of equiaxed solidification might preclude the use of such models in cases with melt inoculation which is often used to enhance heterogeneous nucleation or in similar equiaxed-favoured casting situations [21,23]. To better quantify the influence of the equiaxed growth on the CET, here simulations neglecting equiaxed solidification are run and compared with mixed columnar-equiaxed simulations. With no direct blocking criterion imposed, the columnar tips would grow throughout the length of the 1-D casting sample for the case neglecting equiaxed solidification.

The liquidus isotherm and the columnar tip front as function of the square root of time are plotted in Fig. 9 for the cases of pure columnar growth and mixed columnar-equiaxed growth. The results show that the liquidus isotherms for the two cases are almost identical. The position of the columnar tip front progress almost with the same speed at the initial stage for both cases, but begins to deviate gradually as the columnar tip front approaches the position of CET. The large gap between the liquidus isotherm and the
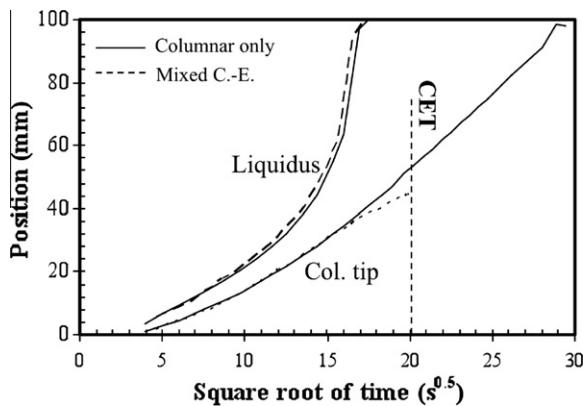
columnar tip front indicates the importance of columnar tip tracking.

The columnar tip growth velocity and cooling rate at the dendrite tip for pure columnar and mixed columnar-equiaxed solidification as function of the columnar tip position are shown in Fig. 10. The CET does not appear to be correlated with any critical columnar tip growth velocity or critical cooling rate. The two simulations show significantly different results with regard to the columnar tip growth velocity and the critical cooling rate at the position of CET (mixed columnar-equiaxed growth).

2.5. Grain sedimentation

To investigate the influence of grain sedimentation on the CET, grain sedimentation and melt convection are included in the calculation. The same geometry configuration, boundary and initial conditions as Fig. 1 are applied. As shown in Fig. 11a, gravity acts in the direction parallel to the heat transfer direction, thus grains fall towards the dendrite tips and into the inter-columnar space. Boussinesq approximation is used to model grain sedimentation by adding a buoyancy force source term, $f_e \cdot \Delta \rho \cdot \bar{g} \cdot \alpha_s^e$, to the momentum equation of the hydrodynamic equiaxed phase, where $\Delta \rho$ is set at 137 kg m^{-3}. Grains are permitted to move within the inter-columnar space if the volume fraction of the columnar phase, f_c, is less than 0.2 [16,17]. Above this critical value the grains are captured between the columnar dendrite trunks and the motion of the equiaxed grains is stopped. Convection due to thermal–solutal buoyancy is neglected but melt convection due to drag from the sinking grains is included. Further details of this grain sedimentation and melt convection model, including interaction of equiaxed grains and growing columnar trunks, can be found elsewhere [16,17].

In Fig. 11b the volume fraction of columnar phase and the velocity vector field of the extradendritic melt are shown, and in Fig. 11c the fraction of equiaxed phase and the equiaxed grain velocity vector field are shown. During solidification the relatively dense equiaxed grains sink and gather near the columnar tip front, displacing the melt in this region and forcing an upward flow of extradendritic melt. As the melt in the inter-columnar space, enriched with solute element, is transported upwards the concentration field is modified, influencing the equiaxed grain nucleation and growth kinetics as well as the growth of the columnar primary dendrite tips. Thus, grain sedimentation impacts not only the equiaxed phase distribution, but also enhances solute and energy transport in the extradendritic melt near the columnar primary dendrite tips. In Fig. 11d the phase and concentration distributions
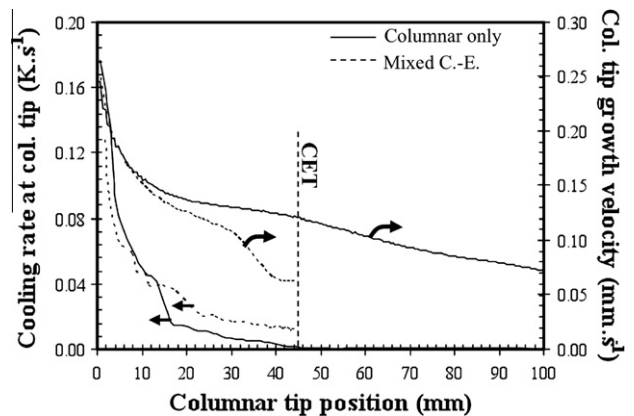

Fig. 9. Numerical result of the liquidus isotherm and the columnar primary dendrite tip position as function of the square root of time. The case of pure columnar growth is compared with the case of mixed columnar-equiaxed growth.

Fig. 10. Comparison of columnar primary dendrite tip growth velocity and corresponding cooling rate at the dendrite tip for pure columnar and mixed columnar-equiaxed growth.
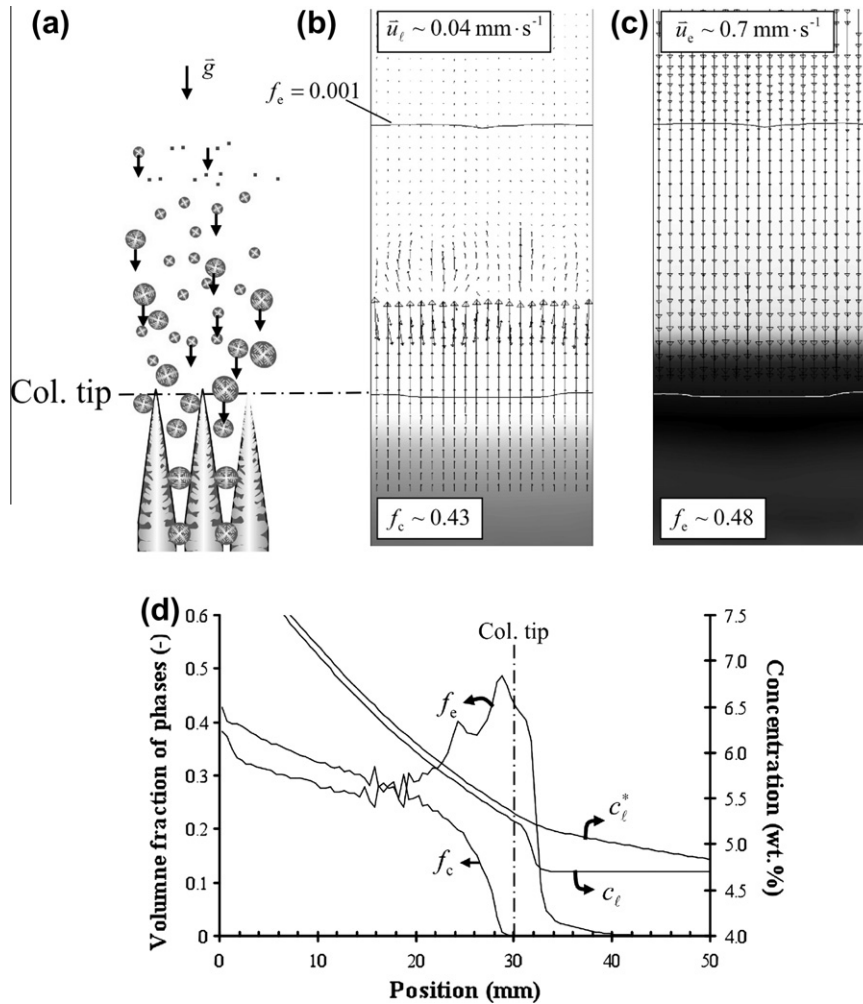
Fig. 11. Unidirectional solidification with grain sedimentation at t = 240 s: (a) schematic of the mixed columnar-equiaxed solidification; (b) columnar fraction, f_c, in gray scale and liquid velocity vectors, $\vec{c}_\ell$; (c) equiaxed fraction, f_e, and equiaxed velocity vectors, $\vec{u}_e$; (d) distribution of f_c, f_e, c_ℓ^* and c_ℓ. All parameters used in this simulation are listed in Table 1; heterogeneous nucleation parameters are: ΔT_N = 5 K, ΔT_σ = 2 K, and n_{max} = 5 × 10^{10} m^{-3}.

of columnar and equiaxed phases, f_c, f_e, c_ℓ^*, and c_ℓ at t = 240 s are shown. In comparison to simulation without sedimentation, Fig. 6, the fraction of equiaxed phase in the inter-columnar region is larger indicating a build-up of falling grains in this region. Additionally, the f_c and f_e curves show small fluctuations due to the flow instabilities induced by sedimentation.

It is surprising to find that, with the inclusion of grain sedimentation and melt convection, using the same solidification conditions of Table 1 with n_{max} equal to 10^9 m^{-3}, the CET is not predicted. Sedimentation of grains, in this case, suppresses the CET as the grains fall into the inter-columnar space, where the equiaxed grain growth is hindered due to spatial constraints. Under the influence of gravity, the falling grains are unable to remain ahead of the columnar tip front long enough to grow to a size in which the hard blocking limit, $f_{e, CET}$ = 0.49, is reached, thus the primary columnar tip growth is not constrained by these falling grains. Additionally, solutal impingement by the growing equiaxed grains in front of the columnar tip front is not sufficiently strong to reduce the growth velocity of the columnar tips. As a result, the CET does not occur in this case. However, when the nucleation parameter, n_{max}, is increased from 10^9 to 5 × 10^{10} m^{-3}, keeping other model inputs unchanged, a larger number of grains nucleate and are able to effectively block the columnar tips through both mechanical and solutal impingement. The CET strongly depends on the number of grains nucleating and growing [11] and this

should be further investigated, however such sensitivity studies are not within the scope of the current work.

To examine the effect of sedimentation on the CET two simulations are compared, with and without grain sedimentation. In each case the equiaxed nucleation parameter n_{max} is 5 × 10^{10} m^{-3} such that CET will occur in the sedimentation case. The evolution of the columnar and equiaxed volume fractions for each case is plotted in Fig. 12. When grain sedimentation is included the CET event occurs earlier (255 s) and with a longer columnar zone (29.8 mm). Without grain sedimentation the CET event occurs later (621 s) and with a shorter columnar zone (18.8 mm). It might be anticipated that the equiaxed grains falling towards the columnar dendrite tip front would enhance mechanical blocking of the columnar dendrite tips and be the primary cause of CET. The current modelling results, however, show that the phase redistribution and enhanced solute mixing caused by grain sedimentation and melt convection significantly promote the growth of the primary dendrite tips, and hence retard the CET. In the case without grain sedimentation, the stationary grains grow in front of the columnar dendrite tip, impeding the growth of primary dendrite tips and decreasing dendrite growth velocity via solutal impingement.

In Fig. 13 the effect of grain sedimentation on the dendritic morphology of the columnar trunks, α_s^c, and equiaxed grains, α_s^e, is shown at t = 300 s. Fig. 13a and b respectively indicate that grain sedimentation has little effect on the dendritic morphology of the
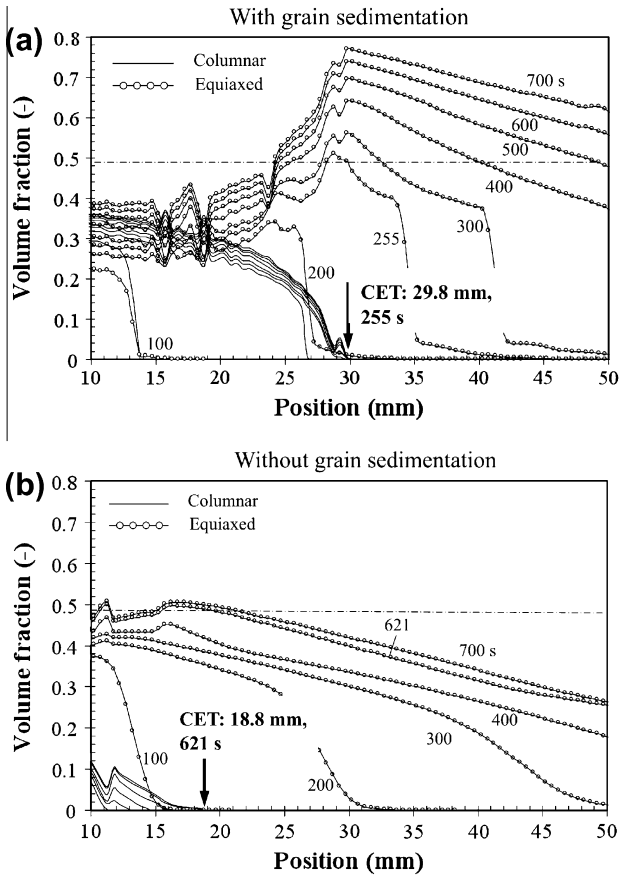
Fig. 12. Comparison of transient columnar, f_c, and equiaxed, f_e, volume fractions over the course of solidification for the cases (a) with grain sedimentation and (b) without grain sedimentation. Nucleation parameters are $n_{max} = 5 \times 10^{10} \, \text{m}^{-3}$, $\Delta T_N = 5 \, \text{K}$, $\Delta T_\sigma = 2 \, \text{K}$. All other boundary and initial conditions for both cases are same.

columnar phase while it significantly influences the dendritic morphology of the equiaxed grains. The sinking grains are predicted to be more dendritic, i.e. α_s^e is smaller, than the globular 'stationary' grains, implying that sedimentation favours dendritic growth in equiaxed grains.

The difference in equiaxed grain dendritic morphology impacts the solutal impingement felt by the growing columnar dendrite tips and is the underlying reason for the difference in columnar dendrite tip velocity. When the equiaxed grains are more globular (no sedimentation) the solute rejected from the solid dendrites into the interdendritic melt is readily transported to the extradendritic melt resulting in significant enrichment of the extradendritic melt. The solute-enriched extradendritic melt decreases the driving force for growth of the columnar primary dendrite tips and the growth velocity of the columnar primary dendrite tips becomes very small as indicated in Fig. 12b. Although the growth of the columnar primary dendrite tips remains active until 621 s, the growth velocity of the columnar primary dendrite tips is so small that the total length the columnar zone grows to only 18.8 mm. In the sedimentation case, the sinking equiaxed grains are more dendritic (Fig. 13b) and most of the solute rejected at the solid–liquid interface during solidification remains enclosed within the interdendritic melt and is not rejected into the extradendritic melt. Thus, solute enrichment in the extradendritic region is much slower and the columnar primary dendrite tip growth is not hindered by solute impingement from the growing equiaxed crystals ahead of the dendrite tip.

Fig. 14 compares the total dendritic solid, $f_s = \alpha_s^e f_e + \alpha_s^c f_c$, that forms during solidification for the cases with and without grain

sedimentation. The thermal boundary conditions for both cases are identical. Given that the heat extraction rate by the casting mould is roughly the same for both cases, the total dendritic solid in each case should also be similar, since the total amount of heat released (the majority coming from solidification latent heat) is balanced with the heat extraction by the casting mould. The total amount of latent heat released is directly correlated to the total dendritic solid, f_s. At 300 s the total solid fraction for each case is roughly equal over the length of the domain. At ~30 mm from the mould wall the total solid volume fraction in the sedimentation case increases slightly in comparison to the case without sedimentation. At 600 s the solid fraction is similar up to 30 mm. At this position, which is the CET in the sedimentation case, the total solid fraction in the sedimentation case jumps in comparison to the case without sedimentation. This could be due to the sedimentation-induced solid phase transport and the enhanced solidification of equiaxed phase caused by the sedimentation-induced mixing.

2.6. Morphological shape factors

Examples of selected dendritic structures and their morphological shape factors are collected in Table 1 of Part I. Here seven cases with different combinations of the morphological shape factors for the columnar trunk and equiaxed grain envelopes are studied, and the predictions of the CET position for each simulation are listed in Table 2. For this parameter study grain sedimentation is not simulated.

When the morphological shape factors of the equiaxed grains are varied, while those of the columnar trunks are constant, as in Cases 1–3, the predicted CET occurs from 42.5 to 58.5 mm from the chilled surface. When the morphological shape factors of the columnar trunks are varied, keeping those of the equiaxed grains constant, as in Cases 4–7, the predicted CET occurs in the range

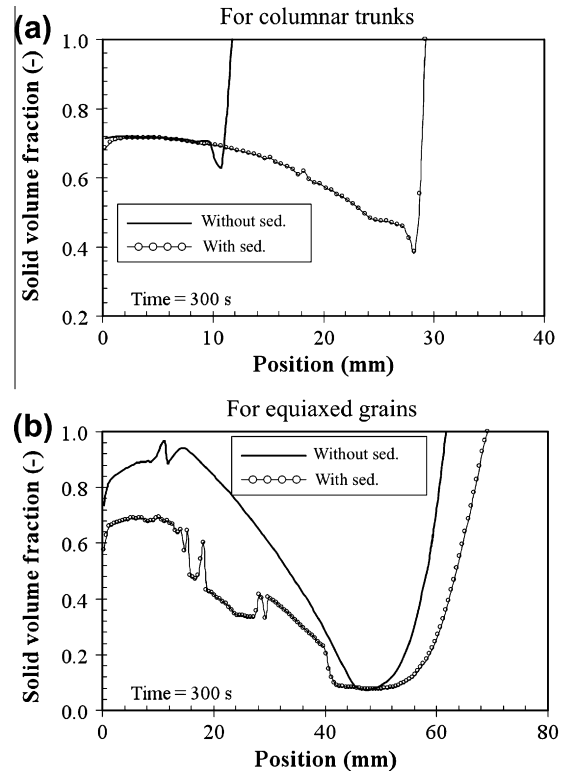**Fig. 13.** Solid volume fraction of: (a) columnar trunks, α_s^c and (b) equiaxed grains, α_s^e, at 300 s. Nucleation parameters are $n_{max} = 5 \times 10^{10} \, \text{m}^{-3}$, $\Delta T_N = 5 \, \text{K}$, $\Delta T_\sigma = 2 \, \text{K}$.
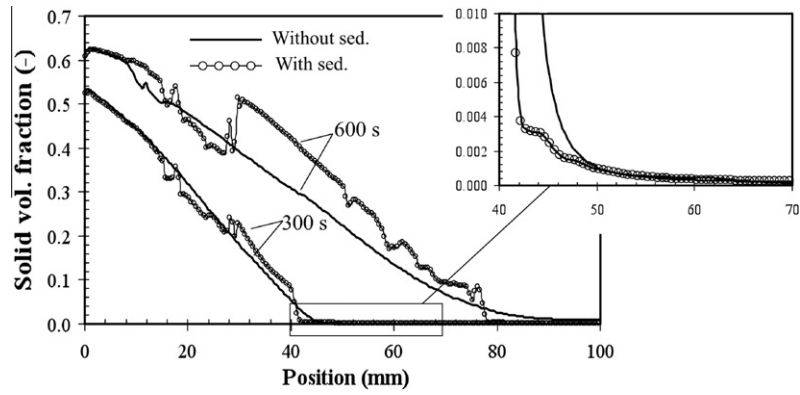
Fig. 14. Predicted solid volume fraction (sum of total dendritic solid: $f_s = \alpha_s^e f_e + \alpha_s^c f_c$) during solidification for simulations with and without sedimentation. Nucleation parameters are $n_{max} = 5 \times 10^{10}$ m^{-3}, $\Delta T_N = 5$ K, $\Delta T_\sigma = 2$ K.

Table 2
Numerical studies of the morphological shape factors.[a]

	Equiaxed grain			Columnar trunk			CET position (mm)
	Shape of envelope	Φ_{env}^e	Φ_{sph}^e	Shape of envelope	Φ_{env}^c	Φ_{circ}^c	
Case 1	Sphere	1	1	OSW4	0.56	0.56	42.5
Case 2	Octah.	0.68	0.85	OSW4	0.56	0.56	49.5
Case 3	OSP6[b]	0.48	0.84	OSW4	0.56	0.56	58.5
Case 4	Mod. octah.	0.68	0.28	Cylinder	1	1	48.5
Case 5	Mod. octah.	0.68	0.28	Square rod	0.80	0.89	47.5
Case 6	Mod. octah.	0.68	0.28	OSW4[c]	0.56	0.56	45.5
Case 7	mod. octah.	0.68	0.28	Mod. quad.	0.80	0.5	44.5

[a] The following boundary conditions and nucleation parameters are kept constant: $T_0 = 932$ K, $H_w = 100$ W m^{-2} K^{-1}, $T_w = 290$ K, $n_{max} = 1 \times 10^9$ m^{-3}, $\Delta T_N = 5$ K, $\Delta T_\sigma = 2$ K.
[b] OSP6: 6 orthogonal square pyramids with pyramid angle 18.43°.
[c] OSW4: 4 orthogonal square wedges with wedge angle 60°.

of 44.5–48.5 mm. These results indicate that the shape of the equiaxed grain envelope has greater influence on the CET than the shape of the columnar trunk envelope. It is also found that the more spherical the equiaxed grain envelope (both Φ_{env}^e and Φ_{sph}^e closer to 1), the shorter the columnar zone that is predicted. This corroborates earlier arguments that equiaxed grains which are more globular reject more solute into the extradendritic melt inducing an earlier CET.
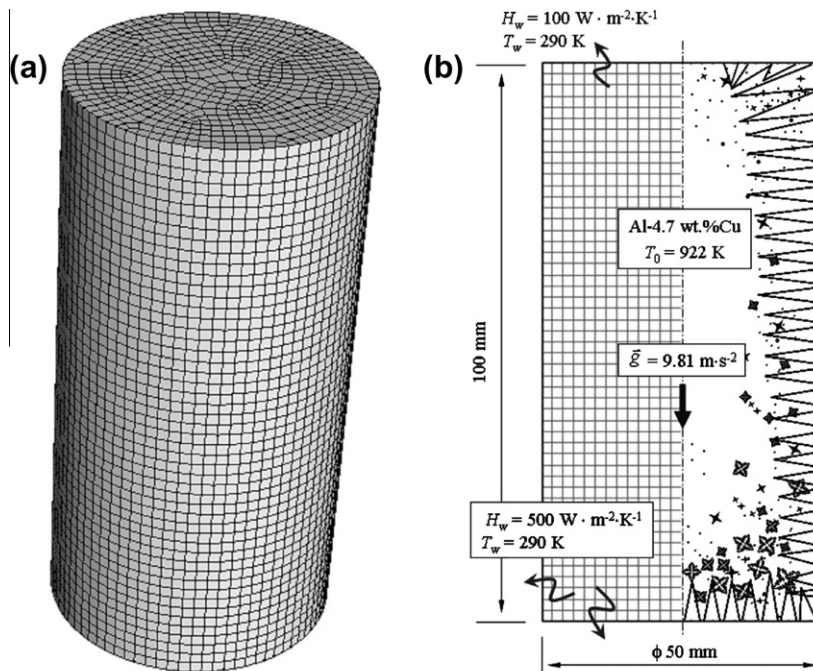

Fig. 15. Schematic of the cylindrical casting and boundary conditions. A 2D axisymmetric calculation and a full 3D calculation for the same casting are carried out: (a) 3D mesh, average mesh size 1.87 mm, number of cells 30,090 and (b) 2D mesh, average mesh size 1.96 mm, number of cells 650.

Table 3
Modelling parameters for the cylindrical casting.

Nucleation parameters	Morphological factors
$n_{max} = 5 \times 10^{10}$ m^{-3}	$\Phi^e_{env} = 0.68$; $\Phi^e_{sph} = 0.28$
$\Delta T_N = 10$ K	$\Phi^c_{env} = 0.80$; $\Phi^c_{circ} = 0.30$
$\Delta T_\sigma = 0.5$ K	$\lambda_1 = 500$ µm; $\lambda_2 = 30$ µm

3. Solidification of a cylindrical casting

3.1. Benchmark description

The applicability of the model to a small ingot casting is demonstrated with a benchmark simulation of a cylindrical casting, φ 50 mm × 100 mm, shown in Fig. 15. To verify the consistency of the numerical model, results from a 2D axisymmetric and a full 3D calculation are discussed and compared. As in the 1D benchmark case, an Al–4.7 wt.% Cu binary alloy is used with the same material properties given in Table 1. The simulation is initialized with 100% liquid at an initial temperature of 922 K. Mould filling is not simulated. Both the mould temperature and the heat transfer coefficient at the mould-casting interface are constant. Growth of columnar primary dendrite trunks is initiated from the bottom and side walls. Grain sedimentation and thermo-solutal convection are modelled with a Boussinesq approximation. Morphological factors and equiaxed grain nucleation parameters are listed Table 3.

3.2. Transient solidification results

Solidification results for the 2D calculation at t = 12.7 s are shown in Fig. 16. The equiaxed and columnar phase distributions and the columnar primary dendrite tip front (overlain in black)

a) $f_e (0 \sim 0.66)$ b) $f_c (0 \sim 0.62)$ c) $M_{\ell c} (0 \sim 196$ d) $M^c_{ds} (0 \sim 14$ e) $M_{\ell e} (0 \sim 188$ f) $M^e_{ds} (0 \sim 88$
$\bar{u}_e (4.0$ mm·s$^{-1})$ $\bar{u}_\ell (1.8$ mm·s$^{-1})$ kg·m^{-3}·s$^{-1})$ kg·m^{-3}·s$^{-1})$ kg·m^{-3}·s$^{-1})$ kg·m^{-3}·s$^{-1})$
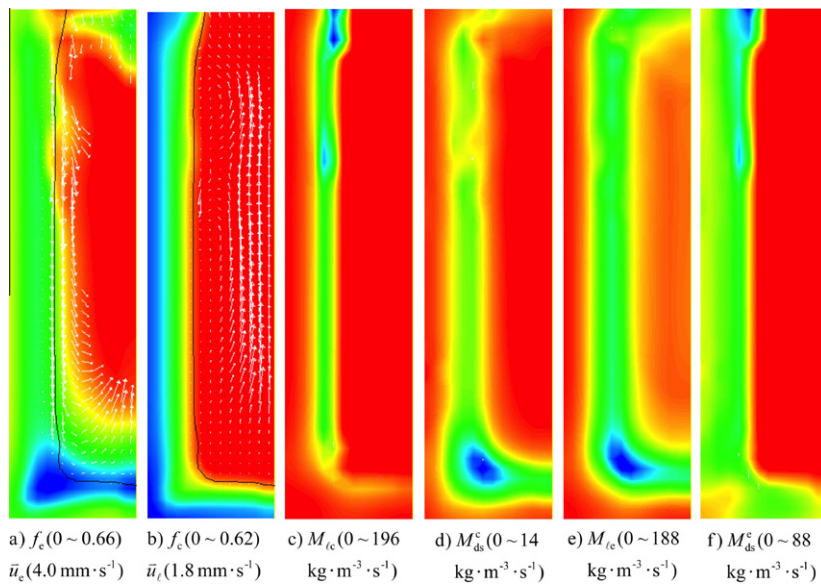
Fig. 16. Snapshot of solidification in 2D axis symmetric simulation at 12.7 s. Each scalar quantity is color scaled with red for the lowest value and blue for the highest with the range shown in parenthesis. Velocity vectors are linearly scaled from 0 to the maximum value shown in parenthesis. The columnar primary dendrite tip front is marked with a black line on: (a) f_e and (b) f_c.
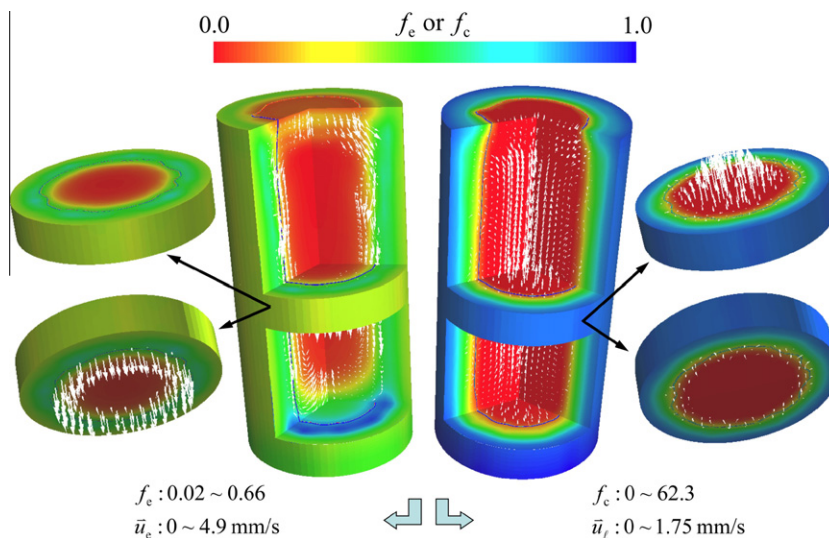

0.0 f_e or f_c 1.0

$f_e : 0.02 \sim 0.66$ $f_c : 0 \sim 62.3$
$\bar{u}_e : 0 \sim 4.9$ mm/s $\bar{u}_\ell : 0 \sim 1.75$ mm/s

Fig. 17. Phase distributions and velocity fields for the 3D ingot simulation at 12.7 s. Phase volume fractions, f_e and f_c, are shown in color scale with red indicating zero and blue indicating the maximum value, the velocity fields $\bar{u}_e$ and $\bar{u}_\ell$ are shown with vectors. The columnar primary dendrite tip front is marked with a black line.

are shown in Fig. 16a and b along with equiaxed and melt velocity vectors. At this early stage of solidification the columnar and equiaxed phases, growing in competition, are found in higher volume fractions near the wall, where the melt is coolest and nucleation initially takes place. The convection patterns, induced by grain sedimentation and thermal–solutal effects, are evident; the growing grains in front of the dendrite tip front sink, dragging liquid melt downwards while inducing a corresponding upward movement of liquid in the centre. Due in part to the small dimension of the casting, the flow is slow, stable, and laminar. Sinking grains that move into the inter-columnar region are trapped if the columnar phase volume fraction is greater than 0.2. This entrapment phenomenon is most prominently observed in the bottom region of Fig. 16a where the equiaxed grains settle.

$M_{\ell c}$, the mass transfer rate from the extradendritic liquid into the columnar phase, and M_{ds}^c, the columnar interdendritic solidification rate, are shown in Fig. 16c and d. These mass transfer rates provide information on the competition between the growth rate of the columnar trunk envelope and the solidification rate of the interdendritic melt. When the growth rate of the envelope is larger than the interdendritic melt solidification rate, the trunk (or grain) becomes more dendritic. Similarly, Fig. 16e and f show $M_{\ell e}$ and M_{ds}^e for the equiaxed growth and the interdendritic melt solidification. The results of the volume fraction of the phases inside the grain envelope (α_s^c, α_d^c, α_s^e, α_d^e) are also available, but not shown here.

The validity of using a 2D axisymmetric model is demonstrated by comparison with results from full 3D simulation shown in Fig. 17a and b. The phase distributions and velocity fields at $t = 12.7$ s are in quantitative agreement with the 2D results; in particular the slow, stable, laminar and axisymmetric nature of the flow indicates that a 2D axisymmetric model geometry is suitable for this size of casting. This consistency applies to all other quantities and remains until the end of solidification.

3.3. Predicted grain structure and macrosegregation

The predicted grain structure and macrosegregation are shown in Figs. 18–20. The model is able to predict important structural information, including volume fraction of columnar and equiaxed phases; the corresponding CET line; the average equiaxed grain size, d^e, and diameter of the columnar trunks, d^c; the eutectic phases formed in the interdendritic region, f_{Eu}^{intern}, and extradendritic region, f_{Eu}^{extra}, including those inside the equiaxed grain envelope and inside the columnar trunk envelope; the total eutectic phase, f_{Eu}^{total}; and the final macrosegregation pattern expressed as c_{mix}. Although model refinements and quantitative validation of the modelling parameters are still required, these numerical predictions agree qualitatively with experimental results often observed in aluminium ingots [3,26]. Systematic quantitative verifications of the model, which include the comparison of the as-cast structures with the numerical predictions, are currently underway. Those verifications together with detailed explanation of the formation of the grain structure will be presented in a subsequent publication.

4. Discussion

The purpose of this work is to propose a mixed columnar-equiaxed solidification model in Part I and to justify the modelling approach and demonstrate model features in Part II. A central objective has been to reproduce the characteristic features of mixed columnar-equiaxed solidification that have been previously verified. To achieve this objective, the current work places significant emphasis on a 1D unidirectional solidification benchmark, which has been intensively studied and is well described in the literature. In a previous study [30] results from the authors' pure equiaxed solidification model results were shown to be in very good agreement with the experiments of Nielsen and co-workers
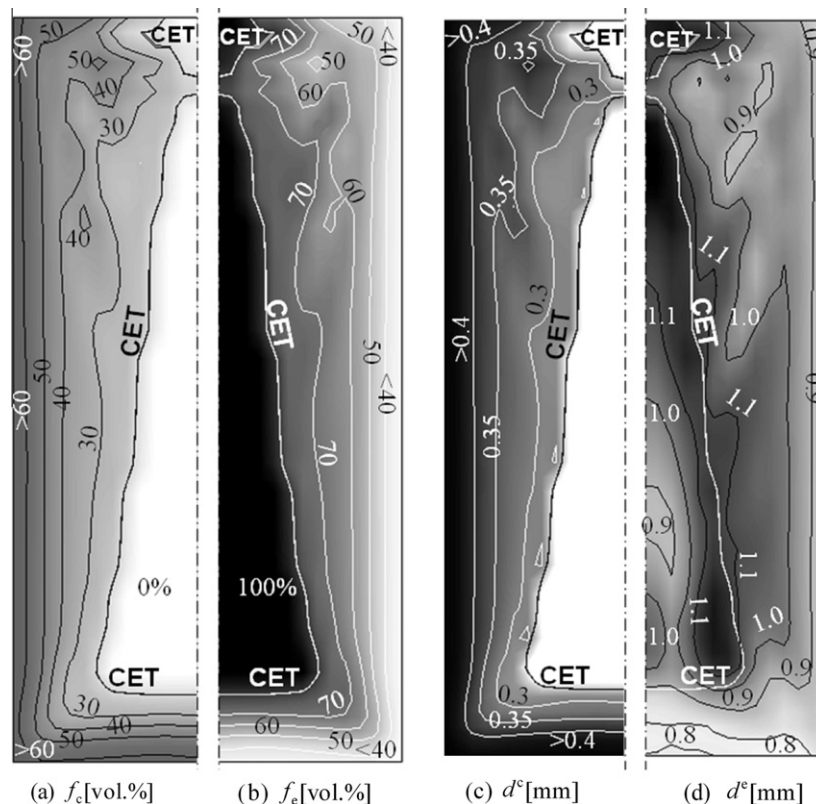

Fig. 18. Predicted grain structure for the 2D axisymmetric simulation. All quantities are shown using gray scale (dark for the highest and light for the lowest value) and isolines. The position of columnar-to-equiaxed transition is indicated with CET line. (a) Volume fraction of the columnar phase; (b) volume fraction of the equiaxed phase; (c) average diameter of the columnar trunks; and (d) average diameter of the equiaxed grains.
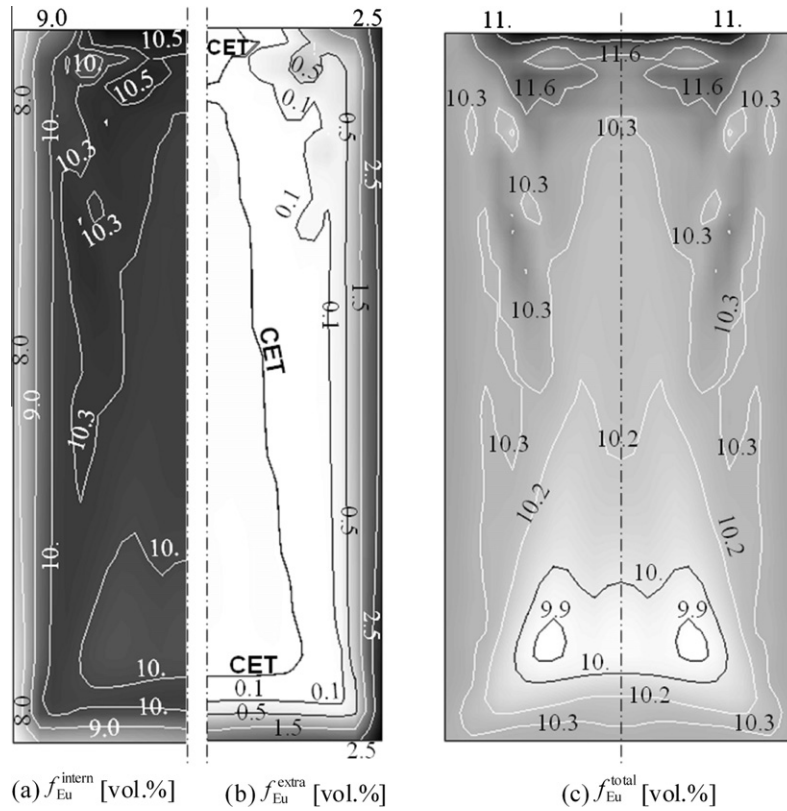
(a) f_{Eu}^{intern} [vol.%]   (b) f_{Eu}^{extra} [vol.%]   (c) f_{Eu}^{total} [vol.%]

Fig. 19. Predicted eutectic phases: (a) volume fraction of the total equiaxed and columnar interdendritic eutectic phase, (b) volume fraction of the extradendritic grain eutectic phase, and (c) volume fraction of the total eutectic phase. All quantities are shown using gray scale (dark for the highest and light for the lowest value) and isolines. The position of columnar-to-equiaxed transition is indicated with CET line.
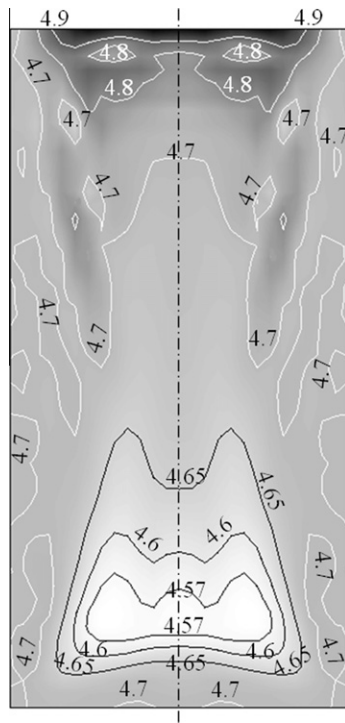

Fig. 20. Final macrosegregation pattern c_{mix} (wt.%) shown using gray scale and isolines.

[31] and the current 2D and 3D calculations of a cylindrical casting show qualitative agreement with classical experiments [26].

4.1. Model potential

The benchmark simulations show that a series of key phenomena accompanying the mixed columnar-equiaxed solidification can be reproduced: the progress of the columnar primary dendrite tip front; the growth of the columnar trunks including the cellular to dendritic growth transition (CDT); the nucleation of the equiaxed grains ahead of the columnar tip front; the growth of the equiaxed grains including the globular-to-dendritic growth transition (GDT); the competition and interaction between the growing equiaxed grains and the columnar dendrites including the columnar-to-equiaxed transition (CET); the grain sedimentation and melt flow, and corresponding influence on global mass, species, energy and momentum transport phenomena; the formation of the interdendritic and extradendritic phases (eutectic); the final macrostructure under the influence of the transport of the phases; and the formation of macrosegregation. The four main difficulties encountered by the previous solidification models as mentioned in Part I have been tackled: (1) bridging the length scales between the global transport phenomena at the process scale with the solidification kinetics governed by the chemical diffusion at the microscopic scale; (2) incorporating different solidification morphologies (globular, cellular, dendritic) into the macro model; (3) including the competition between columnar growth and equiaxed growth and identification of the CET; (4) capturing multiphase transport phenomena including bulk and extradendritic flow and sedimentation of free crystals. As discussed in Part I and here, development of the current model is based on numerous previous works [5–10,13,14]. While treatments for dealing with the above difficulties have been to some extent previously laid out by different authors, the current work integrates them into one model for the first time.

The major contributions of the current work can be summarized as five distinct aspects of the model. (1) Morphological shape factors of the growing crystals are proposed to simplify the dendritic morphology. This simplification makes it possible to implement the complicated dendritic structure of the crystals into the macro model. (2) Independent models for the growth kinetics of the dendritic tips and the solidification of interdendritic melt are incorporated. (3) For columnar solidification, the growth of the primary dendrite tips is modelled with the KGT model [28] and the growth of the secondary dendrite tips are modelled with the LGK model [32]. (4) The columnar tip position is explicitly tracked. (5) The non-uniform solute distribution in the interdendritic melt region is resolved, significantly improving model accuracy and calculation stability [27].

4.2. Model uncertainties and future improvements

The proposed morphological shape factors (Φ_{env}^e, Φ_{sph}^e, Φ_{env}^c, Φ_{circ}^c) have facilitated the coupling of the macro and micro processes, however accurately determining or verifying these factors poses a challenge, particularly because grain morphology is likely to vary with time during solidification. The best way to quantify these factors is to employ numerical methods specialized for microstructural resolution such as phase field [33] or to extract morphological information directly from experimental observations [34]. The current parameter studies shows the sensitivity of the CET position to these factors; based on the unidirectional benchmark (Fig. 1), for the range morphologic configurations simulated (Table 2) the predicted CET position varies from 42.5 mm to 58.5 mm. If the equiaxed grain morphology is kept constant, varying only the columnar trunk morphology, the range in predicted CET position is even smaller (44.5–48.5 mm), indicating the CET results appears to be more sensitive to the equiaxed grain shape factors than the columnar trunk factors. This discrepancy is relatively minor, when compared with the variation in CET due to a change in the nucleation parameter or variation in the heat transfer coefficient at the casting-chill interface or a change in the pouring temperature (superheat). This suggests that the error in CET prediction due to possible erroneous grain morphology assumptions might be smaller than the error resulting from poorly estimated nucleation or thermal parameters.

The diffusion length (thickness of the diffusion layer), l_ℓ, necessary for calculation of the solute diffusion flux around the grain boundary/envelope is an additional factor influencing model accuracy. Assuming that l_ℓ is underestimated, the solute diffusion flux from the interdendritic melt to the extradendritic melt would be overestimated resulting in an underestimation of interdendritic solute enrichment and overestimation of extradendritic enrichment. Consequently the interdendritic solidification rate would be enhanced, and the growth of the grain envelope would be suppressed resulting in more globular grains. Conversely, if the diffusion length around the equiaxed grain envelope is overestimated, the grains would be more dendritic (porous). As the dendritic morphology of the grains is the result of the competition between interdendritic solidification and dendrite tip growth, the estimation of l_ℓ plays an important role in the calculation of the grain dendritic morphology. Numerous formulations for l_ℓ have been suggested by WB [7] and MBG [14] and many other authors [5,6,9,10] with varying degrees of complexity; here the simple formulation of D_ℓ/v_{env} is used to estimate l_ℓ [30] and corrections are made to include the spatial impingement of the grain structures (Part I). Recently, Badillo and co-authors [35,36] have experimentally studied the influence of sedimentation (flow surrounding equiaxed crystal) on the thickness of the diffusion layer in organic materials. Implementation of the results from these studies could improve the current model in this respect.

The hydrodynamic interaction between the equiaxed grains and the columnar trunks is simplified based on an assumption that the equiaxed grains are trapped within the columnar trunks when the local columnar f_c exceeds $f_c^{free} = 0.2$. As discussed previously in the literature [16,17], a suitable physical model has not been found to describe the interaction between the two solid structures in the mixed columnar-equiaxed region. What is certain is that there are the two extremes: when f_c is sufficiently high, the entrapped equiaxed phase cannot move; when f_c is sufficiently low, the equiaxed grains are free to move. There exists a range of f_c, in which a complicated columnar-equiaxed interaction, depending on the dendritic morphology, could operate. In the current model only the two extremes are accounted for and they are assumed to be separated by a critical point f_c^{free}; when f_c is smaller than f_c^{free} the equiaxed grains are free to move, otherwise they are captured. This simple idea has been partially evaluated [17] although further verification is still needed.

Additional model uncertainties and concerns include parameters related to flow-influenced dendritic tip growth and general verification of the model. The influence of flow on the dendritic tip growth kinetics has been found to be significant [33,36], and should be addressed in future model improvements. The preliminary 2D and 3D simulations are not yet sufficient to fully verify the proposed model and complimentary experimental investigations of a cylindrical ingot are currently underway.

4.3. Mixed columnar-equiaxed solidification

Despite the aforementioned uncertainties the current study has demonstrated the potential of the model to accurately describe mixed columnar-equiaxed solidification. Model results allow the subtle details of solidification to be examined, including the competitive aspects of columnar vs. equiaxed growth and tip vs. interdendritic melt solidification; CET predictions; sedimentation and melt convection; and intimate interaction of these phenomena. These are discussed below.

Mixed columnar-equiaxed solidification is characterized by the competing growth of the equiaxed and columnar structures. The growing structures are volume-coupled ($f_e + f_c + f_\ell = 1$), meaning there is spatial impingement as the space being taken by one structure suppresses the growth of the other. In addition there is solutal impingement as the solute diffusion from the envelope of one structure into the shared extradendritic melt suppresses the growth rate of the other structure. As shown in Fig. 5, in the later stages of solidification, the solute enrichment from the growing equiaxed grains will significantly influence the growth of the columnar primary dendrite tips. Mechanical impingement arises when the equiaxed grains ahead of the columnar dendrite tips block the growth of the columnar dendrite tips when the local f_e exceeds a limit of $f_{e,CET}$, as originally implemented by Hunt [11].

A secondary competitive growth phenomenon occurs at the grain level between dendrite tip growth and interdendritic melt solidification. This competition influences the dendritic morphology of the growing structures which in turn can dictate the dominance of either columnar or equiaxed growth. If solidification of the interdendritic melt is favoured and/or the dendrite tip growth is less favoured, the grain structure becomes more globular/cellular. As seen in Fig. 12, highly developed equiaxed dendrites have a larger envelope or 'footprint', suppressing the growth of the columnar dendrites through spatial impingement. Globular grains reject more solute into the extradendritic melt, suppressing columnar growth through solutal impingement.

One of the original goals of CET investigations was to find a criterion to predict the CET for industrial processes. Despite more than 20 years of effort since Hunt [11], this criterion has yet to be established, particularly when grain sedimentation and melt

convection is present. Many authors have proposed indirect criteria for predicting CET [21–25], with varying degrees of success, however these could not be verified by the current model. Additionally the often-used simplification of neglecting equiaxed growth is questionable and current modelling results demonstrate that this simplification results in significant discrepancies, as shown in Figs. 9 and 10. Hunt's analytical model [11] imposed a constant growth velocity $v_{tip'}^c$ and constant temperature gradient G, again an assumption that is only applicable to the unidirectional steady-state solidification, but the CET map created by Hunt's model has been widely verified, and extended to analyze the CET phenomenon in more general cases. A similar CET map is reproduced by the current model (Fig. 8).

In the presence of grain sedimentation, additional phenomena make the CET more difficult to predict. One may anticipate that grain sedimentation in the direction towards columnar tip front would promote CET, as equiaxed grains moving towards the columnar tip front would mechanically hinder the growth of the columnar tips. However, whether this is the case depends on a number of other factors. For example, the 1D sedimentation case with a lower nucleation rate ($n_{max} = 10^9\,\mathrm{m}^{-3}$) has no CET. In comparison, the same simulation without sedimentation does predict a CET. The CET is delayed because the grains near columnar tip sink before they can grow into a blocking scenario. Relatively large amounts of equiaxed grains nucleate at the columnar tip front, due to the large constitutional undercooling. If the grains are stationary, they grow to a certain size and f_e increases. When the local f_e exceeds $f_{e,CET}$ the CET occurs. When sedimentation is included in the model, the large amount of grains located immediately in front of the columnar tip front sink into the inter-columnar space. This process reduces f_e at the columnar tip position and the columnar tip front continues to grow without being blocked, thus CET does not occur.

When a higher nucleation rate is set, $n_{max} = 5 \times 10^{10}\,\mathrm{m}^{-3}$, both cases with and without sedimentation predict CET. The difference is that when sedimentation is neglected the CET event occurs later (621 s) and the columnar zone is shorter (18.8 mm distant from the chilled surface), while when sedimentation is included the CET event occurs earlier (255 s) and the columnar zone is larger (29.8 mm from chilled surface). The columnar tip blocking mechanisms are different for the two cases. In the case with sedimentation the CET occurs relatively early (in time) and is mainly due to mechanical blocking with little influence from solutal impingement. In the case without sedimentation, equiaxed grains located in front of the columnar tips are more globular, and solute impingement due to equiaxed growth is significant, gradually reducing the growth velocity of the columnar tips to zero. In the case of the 1D simulations it can be said that sedimentation phenomenon delays (distance-wise) the CET. In comparison, the simulation results of the cylindrical casting (Figs. 16–18), representing a more realistic situation, show how the equiaxed grains sink and promote the CET in the lower region in comparison to the side and top regions. Thus, a firm general conclusion cannot be drawn in regard to whether the sedimentation phenomenon promotes or suppresses (delays) the CET. As this discussion indicates, the occurrence of the CET depends on numerous factors including the nucleation rate, the grain morphology, and the intensity and direction of the sedimentation.

It is also found that sedimentation influences the dendrite morphology. Fig. 13b demonstrates that the sinking equiaxed grains are more dendritic/porous (smaller α_s^e) than the stationary grains. As mentioned previously, if the grains sink to the cool region, the grain envelope is favoured to grow, however the lower temperature also provides an increased driving force for interdendritic melt solidification. The outcome of the competition between interdendritic melt solidification and the growth of the envelope determines the dendritic morphology of the grains, represented by α_s^e. The result of Fig. 13b indicates that the growth of the envelope, as the grains sink to the cool region, wins the competition over the interdendritic melt solidification. Badillo et al. [35,36] has also found this phenomenon in their sedimentation experiments on organic material (succinonitrile-acetone). Under quasi steady state sedimentation conditions the growing crystal becomes more dendritic with time.

Model consistency is demonstrated among four geometry configurations (0D, 1D, 2D and 3D) and grid studies. The 0D configuration corresponds to a small spherical/cylindrical sample with a given cooling rate in which there is only equiaxed growth and no directional heat transfer, flow and or grain sedimentation, Calculations of this configuration can be verified by comparison with the DSC experiments [27,31]. The results of the mixed columnar-equiaxed solidification on 1D, 2D/3D benchmarks are in agreement with previous modelling results and with the classical experiments [11,26]. To demonstrate grid-independence, calculations were made for two grid sizes, $1 \times 1\,\mathrm{mm}^2$ to $0.5 \times 0.5\,\mathrm{mm}^2$, for the 1D benchmark as discussed in Section 2.1. The phase distributions and transport variables are nearly identical and the difference in the predicted CET positions between the two grids is only 1.25 mm. In the cylindrical casting the 2D axisymmetric calculation with mesh size of 1.96 mm and the full 3D calculation with mesh size of 1.87 mm produced comparable phase distributions and transport variables.

5. Conclusions

A volume-averaging multiphase model for mixed columnar-equiaxed solidification was presented and the following features have been verified:

(1) Key phenomena for the mixed columnar-equiaxed solidification can be modelled including tracking of the columnar primary dendrite tip front; cellular and dendritic growth of columnar trunks including CDT; nucleation of equiaxed grains; globular and dendritic growth of equiaxed grains including GDT; competition and interaction between the growing equiaxed grains and the growing columnar dendrite trunks including CET; grain sedimentation and melt convection and their influence on global mass, species and energy transport; the formation of inter and extradendritic eutectics; and the evolution of grain structures and macrosegregation.
(2) The current model bridges macroscopic transport phenomena with microscopic crystal growth kinetics. This is realized by using a volume-averaging approach and the aforementioned model assumptions/simplifications for the grain morphology. The newly proposed morphological shape factors are critical for this approach and can be quantitatively determined in future work by microstructure modelling techniques, e.g. phase field or experimental investigation.
(3) The ability of the model to deliver consistent results in different geometry configurations (0D, 1D, 2D and 3D) and grid-independence studies is shown.

Based on the illustrative process simulations and parameter studies, the following key aspects of mixed columnar-equiaxed solidification have been demonstrated.

(1) The mixed columnar-equiaxed solidification is characterized by the competition between equiaxed growth and columnar growth, which determines the CET. A secondary growth competition exists between the dendritic tip growth and interdendritic melt solidification, which dictates dendritic

morphology (globular, cellular, and dendritic). The direction in which each of these competitions go, in columnar vs. equiaxed or dendrite tip vs. interdendritic, influences the other. If interdendritic melt solidification is favoured, for instance, the equiaxed grains become more globular, increasing solute rejection into the extradendritic melt. The enhanced solute enrichment of the extradendritic melt by the globular growth suppresses the growth of the columnar tips, which may promote CET.

(2) The CET map created based on the benchmark of unidirectional solidification by varying the process parameters is in agreement with the map from Hunt's model [11].

(3) Whether equiaxed grain sedimentation/floatation promotes or suppresses the CET, depends on the nucleation rate, the dendritic morphology, and the intensity and direction of the sedimentation.

(4) The settling equiaxed grains are predicted to be more dendritic than the 'stationary' grains in agreement with the experimental observations of Badillo et al. [35,36].

The typical grain structure of an Al–Cu cylindrical casting, which was observed experimentally [26], was verified to be reproducible by the current model. Nevertheless, further modelling refinements including verification are still required.

(1) Morphological shape factors will be determined quantitatively. The variation of these factors with time and their influence on the modelling results need further investigation.

(2) Uncertainty about the diffusion length at the grain envelope, l_ℓ, needs further exploration. Alternative diffusion length models [5–10,14,36] could help improve the model in this respect.

(3) The hydrodynamic interaction between the growing columnar dendrites and the equiaxed grains needs further refinement.

(4) Dendrite growth kinetics under the influence of flow [36] should be included in future models.

References

[1] W. Kurz, D.J. Fisher, Fundamentals of Solidification, fourth ed., Trans Tech, Zurich, 1998.
[2] M.-C. Flemings, Solidification Processing, McGraw-Hill, New York, 1974.
[3] A. Ohno, Solidification: The Separation Theory and its Practical Applications, Springer-Verlag, Berlin, 1987.
[4] J. Campbell, Castings, Butterworth-Heinemann Ltd., Oxford, 1991.
[5] M. Rappaz, Ph. Thévoz, Acta Metallurgica 35 (1987) 1487–1497.
[6] M. Rappaz, Ph. Thévoz, Acta Metallurgica 35 (1987) 2929–2933.
[7] C.Y. Wang, C. Beckermann, Metallurgical Transactions A – Physical Metallurgy and Materials Science 24 (1993) 2787–2802.
[8] C.Y. Wang, C. Beckermann, Metallurgical and Materials Transactions A – Physical Metallurgy and Materials Science 27 (1996) 2754–2764.
[9] A.I. Ciobanas, Y. Fautrelle, Journal of Physics D: Applied Physics 40 (2007) 3733–3762.
[10] A.I. Ciobanas, Y. Fautrelle, Journal of Physics D: Applied Physics 40 (2007) 4310–4336.
[11] J.D. Hunt, Materials Science Engineering 65 (1984) 75–83.
[12] M. Gäumann, R. Trivedi, W. Kurz, Materials Science and Engineering A – Structural Materials: Properties, Microstructure and Processing 226–228 (1997) 763–769.
[13] C.Y. Wang, C. Beckermann, Metallurgical and Materials Transactions A – Physical Metallurgy and Materials Science 25 (1994) 1081–1093.
[14] M.A. Martorano, C. Beckermann, Metallurgical and Materials Transactions A – Physical Metallurgy and Materials Science 34 (2003) 1657–1674.
[15] M.A. Martorano, V.B. Biscuola, Acta Materialia 57 (2009) 607–615.
[16] M. Wu, A. Ludwig, Metallurgical and Materials Transactions A – Physical Metallurgy and Materials Science 37 (2006) 1613–1631.
[17] M. Wu, A. Ludwig, Metallurgical and Materials Transactions A – Physical Metallurgy and Materials Science 38 (2007) 1465–1475.
[18] A. Badillo, C. Beckermann, Acta Materialia 54 (2006) 2015–2026.
[19] H.B. Dong, P.D. Lee, Acta Materialia 53 (2005) 659–668.
[20] V.B. Biscuola, M.A. Martorano, Metallurgical and Materials Transactions A – Physical Metallurgy and Materials Science 39 (2008) 2885–2895.
[21] Ch-A. Gandin, Acta Materialia 48 (2000) 2483–2501.
[22] Ch-A. Gandin, ISIJ International 40 (2000) 971–979.
[23] A. McFadden, D.J. Browne, Ch-A. Gandin, Metallurgical and Materials Transactions A – Physical Metallurgy and Materials Science 40 (2009) 662–672.
[24] A. McFadden, D.J. Browne, Applied Mathematical Modelling 33 (2009) 1397–1416.
[25] C.A. Siqueira, N. Cheung, A. Garcia, Metallurgical and Materials Transactions A – Physical Metallurgy and Materials Science 33 (2002) 2107–2118.
[26] R. Morando, H. Biloni, G.S. Cole, G.F. Bolling, Metallurgical Transactions 1 (1970) 1407–1412.
[27] M. Wu, A. Ludwig, Acta Materialia 57 (2009) 5632–5644.
[28] W. Kurz, B. Giovanola, R. Trivedi, Acta Metallurgica 34 (1986) 823–830.
[29] S.Y. Lee, S.M. Lee, C.P. Hong, ISIJ International 40 (2000) 48–57.
[30] M. Wu, A. Ludwig, Acta Materialia 57 (2009) 5621–5631.
[31] Ø. Nielsen, B. Appolaire, H. Combeau, A. Mo, Metallurgical and Materials Transactions A – Physical Metallurgy and Materials Science 32 (2001) 2049–2060.
[32] J. Lipton, M.E. Glicksman, W. Kurz, Materials Science Engineering 65 (1984) 57–63.
[33] I. Stainbach, Modelling and Simulation in Materials Science and Engineering 17 (2009) 1–31.
[34] R.H. Mathiesen, L. Arnberg, F. Mo, T. Weitkamp, A. Snigirev, Physics Review Letters 83 (1999) 5062–5065.
[35] A. Badillo, D. Ceynar, C. Beckermann, Journal of Crystal Growth 309 (2007) 197–215.
[36] A. Badillo, D. Ceynar, C. Beckermann, Journal of Crystal Growth 309 (2007) 216–224.